Influence of oxygen pressure on the fs laser-induced oxidation of molybdenum thin films

NATANAEL CUANDO-ESPITIA,[1] JON REDENIUS,[1] KENDRICK MENSINK,[1] MARCO CAMACHO-LÓPEZ,[2] SANTIAGO CAMACHO-LÓPEZ,[3,4] AND GUILLERMO AGUILAR[1,5]

[1]*Department of Mechanical Engineering, University of California Riverside, Riverside, CA, USA*
[2]*Laboratorio de Investigación y Desarrollo de Materiales Avanzados, Facultad de Química, Universidad Autónoma del Estado de México, Campus Rosedal, Km 14.5 Carretera Toluca-Atlacomulco, San Cayetano de Morelos, Toluca C. P. 50295, México*
[3]*Departamento de Óptica, Centro de Investigación Científica y de Educación Superior de Ensenada, Carretera Ensenada-Tijuana 3918, Zona Playitas, Ensenada, Baja California, 22860, México*
[4]*camachol@cicese.mx*
[5]*gaguilar@engr.ucr.edu*

Abstract: We present a study of femtosecond (1028 nm, 230 fs, 54.7 MHz) laser processing on molybdenum (Mo) thin films. Irradiations were done under ambient air as well as pure oxygen (O_2) at various gauge pressures (4, 8, 12 and 16 psi). Our results indicate that the high heating rates associated with laser processing allow the production of different molybdenum oxides. Raman spectroscopy and scanning electron microscopy are used to characterize the molybdenum oxidation for the different irradiation and oxygen pressures parameters chosen showing a high correlation between well-defined oxidation zones and the oxygen pressure surrounding the samples during the irradiation of the Mo thin films.

References and links

1. S. Deb, "Physical properties of a transition metal oxide: optical and photoelectric properties of single crystal and thin film molybdenum trioxide," Proc. R. Soc. Lond. A Math. Phys. Sci. **304**(1477), 211–231 (1968).
2. H. Gruber and E. Krautz, "Untersuchungen der elektrischen Leitflhigkeit und des Magnetowiderstandes im System Molybdän-Sauerstoff," Phys. Status Solidi **62**(2), 615–624 (1980).
3. G. Blasse and M. Wiegel, "The luminescence of MoO_3 and WO_3: a comparison," J. Alloys Compd. **224**(2), 342–344 (1995).
4. W.-S. Kim, H.-C. Kim, and S.-H. Hong, "Gas sensing properties of MoO_3 nanoparticles synthesized by solvothermal method," J. Nanopart. Res. **12**(5), 1889–1896 (2010).
5. C. Imawan, H. Steffes, F. Solzbacher, and E. Obermeier, "A new preparation method for sputtered MoO_3 multilayers for the application in gas sensors," Sens. Actuators B Chem. **78**(1-3), 119–125 (2001).
6. D. Manno, M. Di Giulio, A. Serra, T. Siciliano, and G. Micocci, "Physical properties of sputtered molybdenum oxide thin films suitable for gas sensing applications," J. Phys. D Appl. Phys. **35**(3), 228–233 (2002).
7. T. Aoki, T. Matsushita, K. Mishiro, A. Suzuki, and M. Okuda, "Optical recording characteristics of molybdenum oxide films prepared by pulsed laser deposition method," Thin Solid Films **517**(4), 1482–1486 (2008).
8. C. G. Granqvist, "Transparent conductive electrodes for electrochromic devices: A review," Appl. Phys., A Solids Surf. **57**(1), 19–24 (1993).
9. K. Bange, "Colouration of tungsten oxide fillms: A model for optically active coatings," Sol. Energy Mater. Sol. Cells **58**(1), 1–131 (1999).
10. C. Julien, G. A. Nazri, J. P. Guesdon, A. Gorenstein, A. Khelfa, and O. M. Hussain, "Influence of the growth conditions on electrochemical features of MoO_3 film-cathodes in lithium microbatteries," Solid State Ion. **73**(3-4), 319–326 (1994).
11. L. C. Yang, Q. S. Gao, Y. Tang, Y. P. Wu, and R. Holze, "MoO_2 synthesized by reduction of MoO_3 with ethanol vapor as an anode material with good rate capability for the lithium ion battery," J. Power Sources **179**(1), 357–360 (2008).
12. G. Ertl, H. Knözinger, and J. Weitkamp, *Handbook of Heterogeneous Catalysis* (1997).
13. E. Gallei and E. Schwab, "Development of technical catalysts," Catal. Today **51**(3-4), 535–546 (1999).
14. S. D. Poletaev, "Laser ablation of thin films of molybdenum for the fabrication of contact masks elements of diffractive optics with high resolution," Proc. Int. Conf. Inf. Technol. Nanotechnol. 82–89 (2015).

15. P. A. Spevack and N. S. Mcintyre, "Thermal Reduction of MoO$_3$," J. Phys. Chem. C **96**, 9029–9035 (1992).
16. M. A. Camacho-López, L. Escobar-Alarcón, M. Picquart, R. Arroyo, G. Córdoba, and E. Haro-Poniatowski, "Micro-Raman study of the m-MoO$_2$ to α-MoO$_3$ transformation induced by cw-laser irradiation," Opt. Mater. (Amst) **33**(3), 480–484 (2011).
17. A. Blume, *Synthese Und Strukturelle Untersuchungen von Molybdän-, Vanadium- Und Wolframoxiden Als Referenzverbindungen Für Die Heterogene Katalyse* (2004).
18. M. Dieterle and G. Mestl, "Raman spectroscopy of molybdenum oxides part1," Phys. Chem. Chem. Phys. **4**(5), 822–826 (2002).
19. I. Navas, R. Vinodkumar, K. J. Lethy, A. P. Detty, V. Ganesan, V. Sathe, and V. P. Mahadevan Pillai, "Growth and characterization of molybdenum oxide nanorods by RF magnetron sputtering and subsequent annealing," J. Phys. D Appl. Phys. **42**(17), 175305 (2009).
20. C. V. Ramana and C. M. Julien, "Chemical and electrochemical properties of molybdenum oxide thin films prepared by reactive pulsed-laser assisted deposition," Chem. Phys. Lett. **428**(1-3), 114–118 (2006).
21. J. Scarminio, A. Lourenço, and A. Gorenstein, "Electrochromism and photochromism in amorphous molybdenum oxide films," Thin Solid Films **302**(1-2), 66–70 (1997).
22. K. Gesheva, A. Szekeres, and T. Ivanova, "Optical properties of chemical vapor deposited thin films of molybdenum and tungsten based metal oxides," Sol. Energy Mater. Sol. Cells **76**(4), 563–576 (2003).
23. S. H. Lee, Y. H. Kim, R. Deshpande, P. A. Parilla, E. Whitney, D. T. Gillaspie, K. M. Jones, A. H. Mahan, S. Zhang, and A. C. Dillon, "Reversible lithium-ion insertion in molybdenum oxide nanoparticles," Adv. Mater. **20**(19), 3627–3632 (2008).
24. Y. Zhang, S. Kuai, Z. Wang, and X. Hu, "Preparation and electrochromic properties of Li-doped MoO$_3$ films fabricated by the peroxo sol-gel process," Appl. Surf. Sci. **165**(1), 56–59 (2000).
25. M. Cano-Lara, S. Camacho-López, A. Esparza-García, and M. A. Camacho-López, "Laser-induced molybdenum oxide formation by low energy (nJ)–high repetition rate (MHz) femtosecond pulses," Opt. Mater. (Amst) **33**(11), 1648–1653 (2011).
26. V. P. Veiko, M. V. Yarchuk, and I. Ivanov, "Mechanisms of thin Cr films modification under multipilse femtosecond laser action," SPIE **7996**, 799607 (2010).
27. V. P. Veiko, M. V. Yarchuk, and A. I. Ivanov, "Study of low-threshold mechanisms for modifying the structure of thin chromium films under the action of supershort laser pulses," J. Opt. Technol. **78**(8), 512–518 (2011).
28. C. Phipps, ed., *Laser Ablation and Its Applications*, Springer Series in Optical Sciences (Springer US, 2007), Vol. **129**.
29. W. Kautek, J. Krüger, M. Lenzner, S. Sartania, C. Spielmann, and F. Krausz, "Laser ablation of dielectrics with pulse durations between 20 fs and 3 ps," Appl. Phys. Lett. **69**(21), 3146–3148 (1996).
30. M. Lenzner, F. Krausz, J. Krüger, and W. Kautek, "Photoablation with sub-10 fs laser pulses," Appl. Surf. Sci. **154**, 11–16 (2000).
31. B. N. Chichkov, C. Momma, S. Nolte, F. von Alvensleben, and A. Tünnermann, "Femtosecond, picosecond and nanosecond laser ablation of solids," Appl. Phys., A Mater. Sci. Process. **63**(2), 109–115 (1996).
32. K. Sugioka, M. Meunier, and A. Piqué, *Laser Precision Microfabrication* (2010), Vol. 135.
33. M. Rouhani, Y. L. Foo, J. Hobley, J. Pan, G. S. Subramanian, X. Yu, A. Rusydi, and S. Gorelik, "Photochromism of amorphous molybdenum oxide films with different initial Mo5+ relative concentrations," Appl. Surf. Sci. **273**, 150–158 (2013).
34. M. Rouhani, J. Hobley, G. S. Subramanian, I. Y. Phang, Y. L. Foo, and S. Gorelik, "The influence of initial stoichiometry on the mechanism of photochromism of molybdenum oxide amorphous films," Sol. Energy Mater. Sol. Cells **126**, 26–35 (2014).
35. G. Heise, M. Englmaier, C. Hellwig, T. Kuznicki, S. Sarrach, and H. P. Huber, "Laser ablation of thin molybdenum films on transparent substrates at low fluences," Appl. Phys., A Mater. Sci. Process. **102**(1), 173–178 (2011).
36. J. Hermann, M. Benfarah, S. Bruneau, E. Axente, G. Coustillier, T. Itina, J.-F. Guillemoles, and P. Alloncle, "Comparative investigation of solar cell thin film processing using nanosecond and femtosecond lasers," J. Phys. D Appl. Phys. **39**(3), 453–460 (2006).
37. S. Bashir, M. S. Rafique, C. S. Nathala, A. A. Ajami, and W. Husinsky, "Femtosecond laser fluence based nanostructuring of W and Mo in ethanol," Phys. B Condens. Matter **513**, 48–57 (2017).
38. M. Domke, S. Rapp, M. Schmidt, and H. P. Huber, "Ultra-fast movies of thin-film laser ablation," Appl. Phys., A Mater. Sci. Process. **109**(2), 409–420 (2012).
39. M. A. Py, P. E. Schmid, and J. T. Vallin, "Raman scattering and structural properties of MoO$_3$," Nuovo Cim. B Ser. 11 **38**(2), 271–279 (1977).
40. J. P. Thielemann, G. Weinberg, and C. Hess, "Controlled Synthesis and Characterization of Highly Dispersed Molybdenum Oxide Supported on Silica SBA-15," ChemCatChem **3**(11), 1814–1821 (2011).
41. N. Floquet, O. Bertrand, and J. J. Heizmann, "Structural and morphological studies of the growth of MoO3 scales during high-temperature oxidation of molybdenum," Oxid. Met. **37**(3-4), 253–280 (1992).
42. P. A. Spevack and N. S. McIntyre, "A Raman and XPS investigation of supported molybdenum oxide thin films. 1. Calcination and reduction studies," J. Phys. Chem. **97**(42), 11020–11030 (1993).
43. M. Cano-Lara, "Tesis defendida por Miroslava Cano Lara y aprobada por el siguiente comité Dr. Santiago Camacho López," CICESE (2013).
44. S. He, S. Amoruso, D. Pang, C. Wang, and M. Hu, "Chromatic annuli formation and sample oxidation on copper

thin films by femtosecond laser," J. Chem. Phys. **144**(16), 164703 (2016).

45. M. Shimizu, M. Sakakura, M. Ohnishi, Y. Shimotsuma, T. Nakaya, K. Miura, and K. Hirao, "Mechanism of heat-modification inside a glass after irradiation with high-repetition rate femtosecond laser pulses," J. Appl. Phys. **108**(7), 073533 (2010).

46. S. I. Anisimov, B. L. Kapeliovich, and T. L. Perel-man, "Electron emission from metal surfaces exposed to ultrashort laser pulses," J. Exp. Theor. Phys. **66**, 375–377 (1974).

47. L. Kotsedi, K. Kaviyarasu, X. G. Fuku, S. M. Eaton, E. H. Amara, F. Bireche, R. Ramponi, and M. Maaza, "Two temperature approach to femtosecond laser oxidation of molybdenum and morphological study," Appl. Surf. Sci. **421**, 213–219 (2016).

48. L. L. Y. Chang and B. Phillips, "Phase Relations in Refractory Metal-Oxygen Systems," J. Am. Ceram. Soc. **52**(10), 527–533 (1969).

49. R. Weber, T. Graf, P. Berger, V. Onuseit, M. Wiedenmann, C. Freitag, and A. Feuer, "Heat accumulation during pulsed laser materials processing," Opt. Express **22**(9), 11312–11324 (2014).

50. A. T. Nelson, E. S. Sooby, Y. J. Kim, B. Cheng, and S. A. Maloy, "High temperature oxidation of molybdenum in water vapor environments," J. Nucl. Mater. **448**(1-3), 441–447 (2014).

51. J. F. Ready, *Effects of High-Power Laser Radiation* (Academic Press, Inc., 1971).

52. A. Hojabri, F. Hajakbari, A. Emami Meibodi, and M. Moghri Moazzen, "Influence of Thermal Oxidation Temperatures on the Structural and Morphological Properties of MoO_3 Thin Films," Acta Phys. Pol. A **123**(2), 307–308 (2013).

53. M. L. Colaianni, J. G. Chen, W. H. Weinberg, and J. T. Yates, Jr., "Oxygen on Mo(110): low-temperature adsorption and high-temperature oxidation," Surf. Sci. **279**(3), 211–222 (1992).

54. B. Sundqvist and G. Bäckström, "Thermal conduction of metals under pressure," Rev. Sci. Instrum. **47**(2), 177–182 (1976).

55. Q. Wang, A. Chen, S. Li, H. Qi, Y. Qi, Z. Hu, and M. Jin, "Influence of ambient pressure on the ablation hole in femtosecond laser drilling Cu," Appl. Opt. **54**(27), 8235–8240 (2015).

56. R. Yan, J. R. Simpson, S. Bertolazzi, J. Brivio, M. Watson, X. Wu, A. Kis, T. Luo, A. R. Hight Walker, and H. G. Xing, "Thermal conductivity of monolayer molybdenum disulfide obtained from temperature-dependent Raman spectroscopy," ACS Nano **8**(1), 986–993 (2014).

1. Introduction

Numerous transition-metal oxides have begun to attract the consideration of engineers and scientists in the chemical, physical, and material science realm. Specifically, molybdenum oxides such as MoO_2 (molybdenum IV), and MoO_3 (molybdenum VI) have gained attention due to their optical and electronic properties [1–3]. Some of the technological applications of molybdenum oxides include gas sensing [4–6], optical recording [7] and electrochromic devices [8,9]. Moreover, molybdenum oxides have been used as cathode material in micro-batteries [10,11], in partial oxidation of hydrocarbons [12,13] and as micro masks in diffractive optics elements [14]. Raman spectroscopy has been used to identify different molybdenum oxidation states such as monoclinic MoO_2 (m-MoO_2) [15–17], orthorhombic Mo_4O_{11} (o-Mo_4O_{11}) [17,18], monoclinic Mo_8O_{23} (m-Mo_8O_{23}) [17,19], orthorhombic $Mo_{18}O_{52}$ (o-$Mo_{18}O_{52}$) [17] and orthorhombic MoO_3 (α-MoO_3) [15,16,19]. Table 1 summarizes the Raman peaks reported in literature for the molybdenum oxides mentioned above.

Many deposition techniques have been reported to form molybdenum and molybdenum oxide thin films, including Pulsed Laser Deposition [20], RF Magnetron sputtering [19,21], Chemical Vapor Deposition [22,23] and wet chemistry methods [24]. It has been recently shown by our group [25] and others [26,27] that pulsed femtosecond lasers can produce specific oxides when irradiated on a metallic thin film. In contrast to conventional thermal oxidation, laser-induced oxidation allows material processing with micrometer resolution and a great control over the oxidation species obtained by adjusting the laser parameters used. Moreover, the processing precision achieved by using ultrashort laser pulses in machining semiconductors and metals have been unexpectedly high [28–30]. With femtosecond laser pulses, the energy may be deposited in the material in a period of time shorter than the relaxation time between the electron and the lattice system [31]. This in turn may allow processes like vaporization or oxidation to occur before electron and lattice systems reach thermal equilibrium (see chapter 8 of [32]). This is of particular interest as thin film metal oxides are being used in many different innovative technologies. Gesheva et al. [22] have studied molybdenum and tungsten oxide films because of their electrochromatic tunability for a given electrical charge. Rouhani et al. [33,34] have begun a study on which molybdenum

ion and oxygen vacancies are responsible for the colorization and photochromism of MoO_3 thin films. Heise et al. [35] have used picosecond lasers to selectively structure the molybdenum electrodes currently used in CIS thin film solar cells. We have shown in a previous report that scans from a femtosecond laser on molybdenum thin films in ambient air oxidize the local target area [25]. However, it has yet to be seen how different oxygen pressures can affect the resulting oxides based on varying laser irradiation parameters. Studying laser irradiation under different oxygen pressures will help to further elucidate the oxidation mechanism but also to experimentally explore the possible morphologies and structures obtained by varying oxygen pressure during laser irradiations. In this work, we present a systematic study of femtosecond laser irradiation on molybdenum thin films; varying oxygen pressure shows considerable differences in the processing results for thin film oxidation.

Table 1. Reported Raman peaks of molybdenum oxides [cm^{-1}]

α-MoO$_3$			m-MoO$_2$			o-Mo$_4$O$_{11}$		m-Mo$_8$O$_{23}$		o-Mo$_{18}$O$_{52}$
Ref [15]	Ref [19]	Ref [16]	Ref [15]	Ref [16]	Ref [17]	Ref [18]	Ref [17]	Ref [17]	Ref [19]	Ref [17]
219	220	217	203	203	208	206	208	208	222	208
244	246	245	208	208	232	229	253	256	245	465
285	290	284	228	229	353	264	281	282	373	547
293	337	291	345	346	370	306	339	309	592	622
338	378	338	363	350	448	340	359	338	654	637
379	473	365	461	365	473	380	380	352	875	679
470	668	379	495	459	501	431	413	377	918	761
668	820	472	571	469	572	452	435	394	951	906
821	875	666	589	496	590	498	454	432		931
997	902	820	744	569	748	568	714	480		951
	921	996		588		744	787	668		972
	953			744		790	837	709		989
	996					835	892	733		1001
	1009					843	916	811		
						907	963	880		
						985		899		

2. Materials and methods

2.1 Molybdenum thin films

Molybdenum thin films were deposited by using the magnetron DC-sputtering technique. A disk of molybdenum (99.9%, Lesker) was used as target and argon gas to sputter it. Molybdenum was deposited on fused silica substrates at room temperature. The as-deposited molybdenum thin films were characterized by XRD and SEM obtaining a very smooth and homogeneous surface of (110) molybdenum. Detailed information about the synthesis and characterization methods can be found in previous reports [25]. The thickness of the films (500 nm) was measured by profilometry and confirmed by SEM. The molybdenum thin films were cut using a glass cutter and cleaned in an acetone bath ultrasonication. The films were cut into small centimeter-by-centimeter squares to be able to fit onto the mount inside a custom gas chamber. Once attached, the samples were cleaned again using acetone and methanol. The chamber was then sealed to prepare for the various atmospheric conditions before laser irradiation.

2.2 Experimental setup

In our experiments, we used a femtosecond laser oscillator (Mikan, Amplitude Systems) delivering pulses of 230 fs, with maximum energy per pulse of 20 nJ, and centered at 1028 nm to irradiate molybdenum thin films at a repetition rate of 54.7 MHz. We carried out the laser irradiation of the films at normal incidence and focused down the incident laser beam by

means of an aspheric lens of 15.29 mm focal length; which gave a beam waist ($1/e^2$) of about 19 µm. The films and chamber were conveniently mounted on a computer controlled XY stage and kinematic mount. A linear polarizer and a half-wave plate were used to control the energy delivered to the thin films, while a shutter controlled laser exposure time. Figure 1 schematically shows the experimental setup used in the experiments reported here. In this study fluences from 0.29 to 2.14 mJ/cm^2 and exposure times from 1 to 10 s were used at static locations on the thin films. Fluences in the range of few mJ/cm^2 are well below the ablation threshold of molybdenum reported previously in vacuum [36] as well as the fluences recently used in studies on femtosecond laser nanostructuring of molybdenum [37,38].
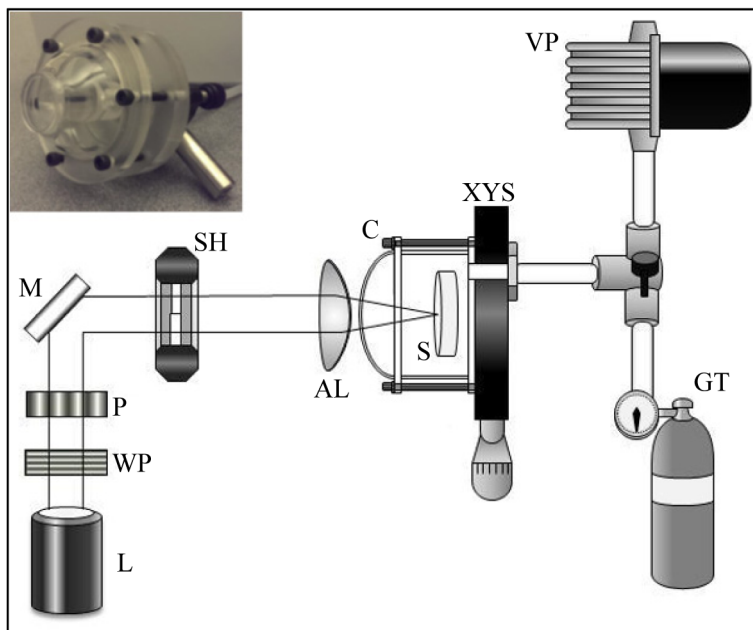
Fig. 1. Schematic representation of the experimental setup. L: laser, WP: wave plate, P: polarizer, M: mirror, SH: shutter, AL: aspheric lens, C: chamber, S: sample, XYS: XY stage, GT: gas tank, VP: vacuum pump. The inset shows a picture of the chamber where the thin films were laser irradiated.

To create different oxygen pressures, a robust chamber was constructed. The chamber uses a quartz window with a flat incident exposure area on top of a dome (see inset of Fig. 1). The spherical chamber was then mounted onto a plastic backing which included a gas inlet. An O-ring on the chamber-mount interface ensured the atmospheric seal. The experiments were run under different oxygen pressure conditions, which were achieved by extracting air via a diaphragm vacuum pump (Edwards, United Kingdom). These conditions were verified using a vacuum gage; measuring down to 29 In-Hg (98% vacuum). Then, a three-way valve was used to push pure oxygen gas via the same tube into the chamber. The chamber was evacuated and refilled with oxygen gas a total of three times before laser experiments. The oxygen gauge pressures used were 4 psi, 8 psi, 12 psi, and 16 psi which correspond to absolute pressures of 129, 157, 184 and 212 kPa respectively. Finally, irradiations with different energies, exposure times and oxygen pressures were performed.

3. Results and discussion

3.1 Molybdenum oxides regions

After laser irradiation, we observed a rich structural and morphological change in the molybdenum thin films. Figures 2(a) and 2(b) show two representative micrographs of the

laser-modified thin films after 10 s of laser irradiation with a fluence of 0.58 mJ/cm^2. While the sample shown in Fig. 2(a) was irradiated in ambient air conditions, the sample depicted in Fig. 2(b) was irradiated in 16 psig pressurized oxygen. As seen in Fig. 2(a), several zones can be clearly distinguished by surface morphology and coloration. The central circular region in Figs. 2(a) and 2(b) has been labeled as "I" in both micrographs. Blue and green-gray colors can be observed in region I of Fig. 2(a) (ambient air) while dark-teal colors are observed in region I of Fig. 2(b) (16 psig). A difference between this central region and the corresponding adjacent outer region (II for Fig. 2(a), III for Fig. 2(b)) is clear from the optical images as well as from SEM images (see Figs. 2(c) and 2(d)).
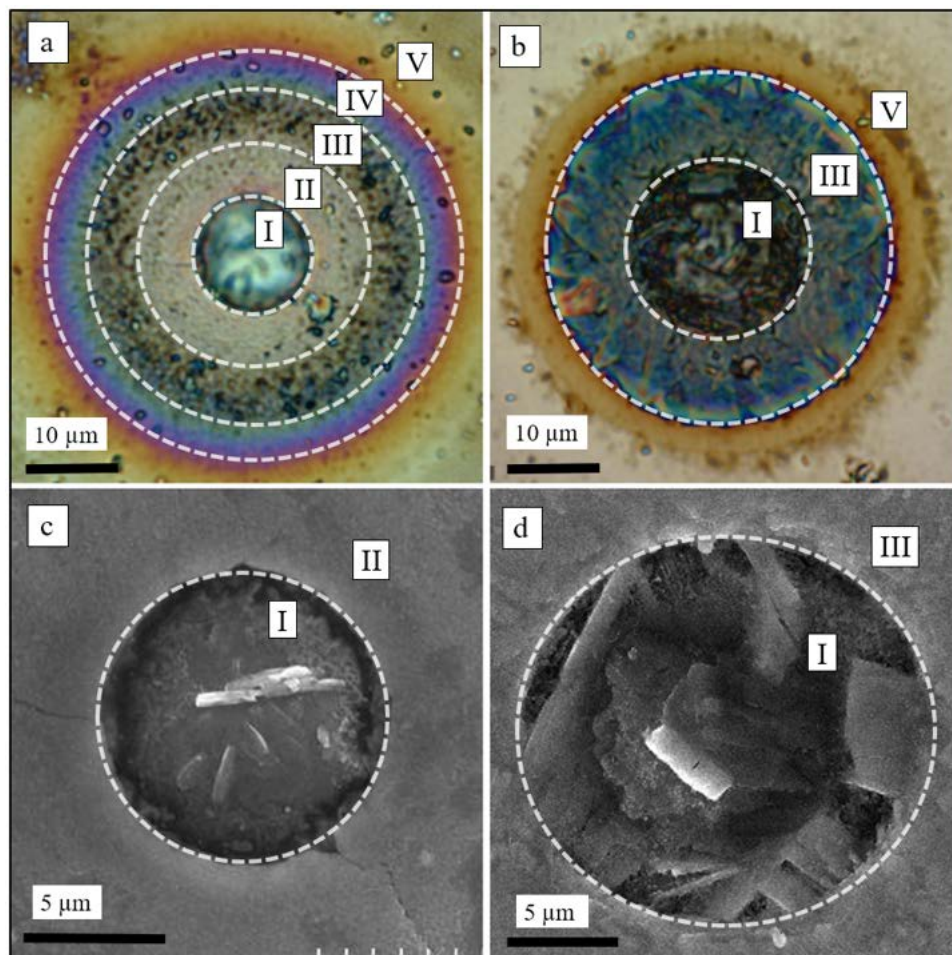
Fig. 2. Micrographs of irradiated molybdenum thin films (0.58 mJ/cm^2, 10 s) in atmospheric air (a) and 16 psig O$_2$ (b). c-d: SEM images from samples depicted in a-b, respectively. Different modified regions can be observed (labeled as I, II, III IV and V). The images suggest a crater-like morphology and crystallites in the inner region.

Raman spectra (LabRaman HR-800 of Jobin–Yvon-Horiba) from region I shows peaks at 195, 217, 245, 284, 282 338, 365, 666, 820, and 996 cm^{-1} which highly correlate with the peaks associated with the α-MoO$_3$ crystalline phase [15–17,39,40]. Raman peaks from region I were very similar for both ambient air and pressurized oxygen irradiation experiments. A representative Raman spectrum from region I is shown in Fig. 3 with a characteristic dominating peak at 820 cm^{-1}. Additionally, Fig. 3 also shows a representative Raman spectrum for the different regions observed in the light micrographs of Fig. 2. Again, Raman

peaks from region III were very similar for both ambient air and pressurized oxygen irradiation experiments. SEM images from Fig. 2 reveal formation of platelet crystallites inside region I. In accordance with Floquet et al, this morphology corresponds to α-MoO$_3$ [41], which supports the results of Raman spectroscopy and evidences the notable differences on the oxidation structures obtained by means of ultrashort laser irradiation.
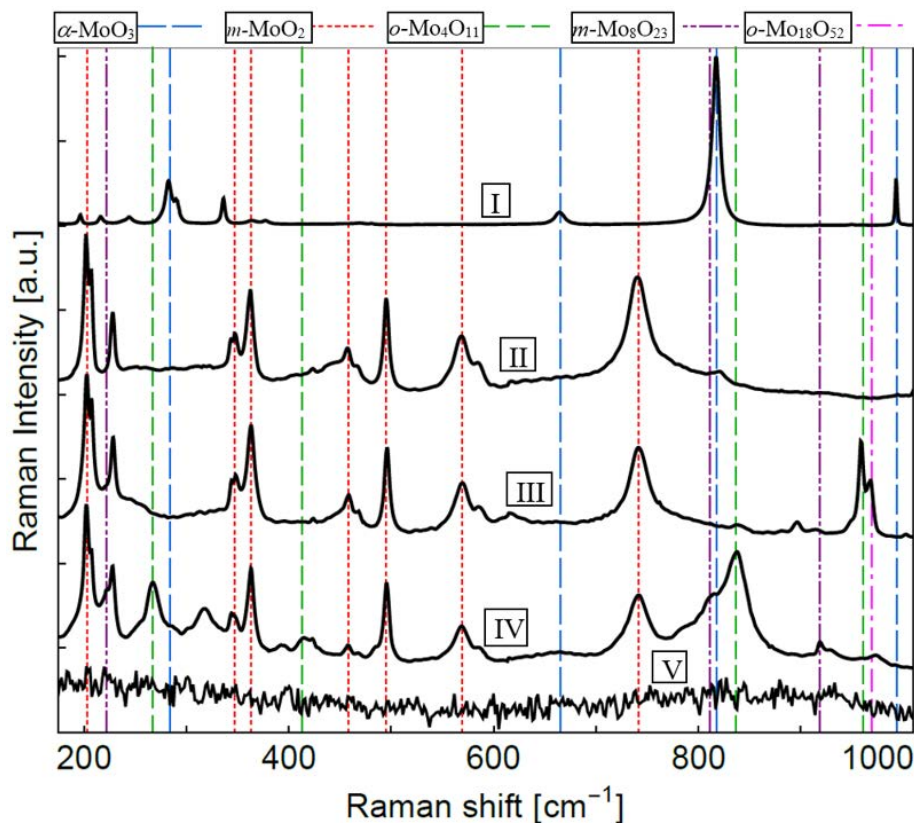

Fig. 3. Representative Raman spectra for the different regions shown in Fig. 2. Some of the characteristic peaks of molybdenum oxides have been highlighted.

The region labeled as II in Fig. 2(a) shows a uniform brown-gray color and its Raman spectra contains the characteristic peaks at 203, 207, 228, 345, 363, 461, 495, 571, 589, and 744 cm^{-1} associated with monoclinic MoO$_2$ (m-MoO$_2$) phase [16,17]. For some of the samples studied, a small peak at 820 cm^{-1} was observed in this region which indicates a content of α-MoO$_3$. Region III in Fig. 2(a) shows a grainy brown-gray coloration. For region III, we have found similar Raman spectra to region II with additional peaks at 837, 897, 961 and 970 cm^{-1}. These peaks can be related with the o-Mo$_4$O$_{11}$ and o-Mo$_{18}$O$_{52}$ phases (see Table 1). On the other hand, region III from Fig. 2(b) shows a homogeneous blue-light teal coloration. Although the difference in coloration, region III from Fig. 2(a) and region III from Fig. 2(b) share similar features of their corresponding Raman spectra showing a dominating content of m-MoO$_2$ with some content of o-Mo$_4$O$_{11}$ and o-Mo$_{18}$O$_{52}$.

Finally, the region labeled in Fig. 2(a) as IV shows a complex coloration with light blue-green at the inner annuli followed by blue then purple and brown-red at the outer annuli. The coloration pattern in region IV showed high consistency over the irradiations studied in this work. The Raman spectra of this region has shown the corresponding peaks of m-MoO$_2$ with peaks at 267, 319, 413 and 837 cm^{-1} which correspond to o-Mo$_4$O$_{11}$ except for 319 cm^{-1}; and peaks at 222, 811 and 919 cm^{-1} which can be related with the m-Mo$_8$O$_{23}$ molybdenum phase

(see Table 1). Although each color seen in region IV may be associated with a corresponding molybdenum phase, a higher spatial resolution (<5μm) is needed while acquiring the Raman spectrum to elucidate these possible features. In general, we have seen that region IV exhibits smaller areas for samples irradiated in pressurized oxygen than in atmospheric air conditions. Figure 2(b) depicts a case in which the complex coloration annuli is very faint and thus region IV is not labeled in Fig. 2(b). In the outermost regions (labeled as V) with light brown coloration we did not find any characteristic Raman signal as shown in the corresponding Raman spectrum of Fig. 3. The Raman spectrum obtained from region V is the expected Raman spectrum of an amorphous metal like molybdenum [42]. This suggests an unoxidized amorphous molybdenum region outside region IV which in turn delimits the laser-modification area for a given fluence, irradiation time and atmospheric conditions. Similar coloration patterns have been reported in fs laser scans and static irradiation on molybdenum thin films in air [43]. Femtosecond laser-induced chromatic phenomena has been explained as the result of nanoparticle formation with different crystalline states [44] and as the degree of oxidation and phase change of the irradiated material [25]. Due to its relationship with the thermally-modified boundary, we believe that complex coloration annuli formation is triggered by the thermal gradient imposed in the material surface during laser irradiation. Light microscopy images in Fig. 4 show the morphological and annuli colorization effects on molybdenum thin films from two fluences and two atmospheres for 1, 3, 5, and 10 seconds of laser exposure.

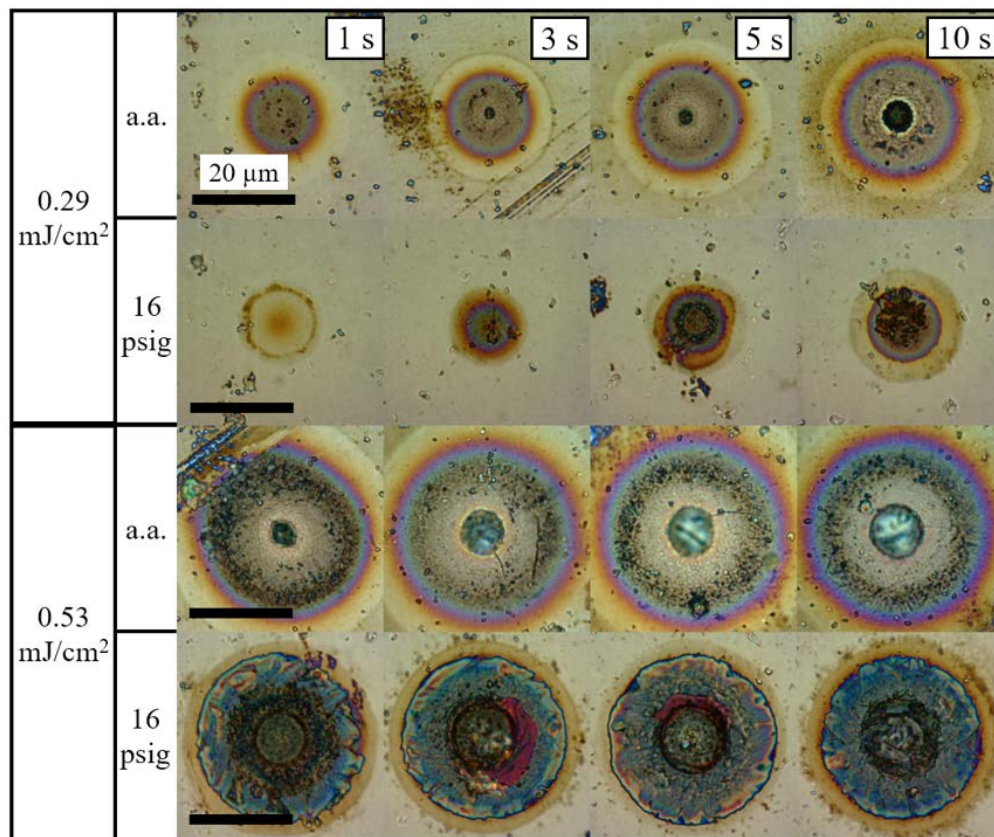### 3.2 Influence of irradiation time on laser-induced oxidation

Fig. 4. Light micrographs of molybdenum thin films irradiated for 1, 3, 5 and 10 seconds. Two sets of fluences (0.29 and 0.53 mJ/cm²) and two atmosphere conditions, ambient air (a.a.) and pressurized oxygen at 16 psig are depicted. The scale bar corresponds to 20 μm.

The images shown in Fig. 4 were selected to evidence the distinct impact of the pressurized oxygen conditions on the final features of laser irradiated molybdenum thin films. On the first two rows of Fig. 4 the images for a fixed laser fluence (0.29 mJ/cm^2) are shown for samples irradiated in ambient air (first row) as well as for samples irradiated at 16 psig pressurized oxygen atmosphere (second row). Remarkably, according to the first two rows of Fig. 4, the incorporation of more oxygen atoms in the experimental atmosphere leads to a smaller affected area. Although the physics underlying the interaction of femtosecond laser pulses with metal thin films is very complex and cannot be directly addressed by means of basic experiments like the ones presented in this work, we will elaborate in the following sections on the possible mechanisms involved in this counterintuitive result.

By comparing the first column of Fig. 4 one can notice that another effect of the pressurized oxygen condition is to delay the appearance of well-formed oxidation regions. After 1 second of irradiation, the sample irradiated in ambient air with a fluence of 0.29 mJ/cm^2 (first row, first column of Fig. 4) shows a coloration associated with m-MoO$_2$/o-Mo$_4$O$_{11}$/o-Mo$_8$O$_{23}$ phases (see Fig. 2 and Fig. 3) while for the same irradiation time and same fluence the sample irradiated at 16 psig pressurized oxygen (second row, first column of Fig. 4) only shows a faint light-brown coloration which is characteristic of amorphous molybdenum with no oxidation. For the same irradiation time (1 s) but 0.53 mJ/cm^2 fluence, the thin film irradiated in ambient air as well as the thin film irradiated at 16 psig pressurized oxygen (third and fourth rows, first column of Fig. 4) show all the regions described in Fig. 2. This indicates that the minimum fluence needed to start oxidation after 1 second of irradiation is less than 0.29 mJ/cm^2 for the case of ambient air and between 0.29 mJ/cm^2 and 0.53 mJ/cm^2 for the case of 16 psig pressurized oxygen. Similarly, the first two rows of Fig. 4 show that for the fixed fluence of 0.29 mJ/cm^2, the irradiation time needed to start oxidation is less than 1 second for the case of ambient air and between 1 and 3 seconds for the case of 16 psig pressurized oxygen. On the other hand, the last two rows of Fig. 4 show optical micrographs corresponding to samples irradiated under ambient air and 16 psig pressurized oxygen conditions for a fixed fluence of 0.53 mJ/cm^2. For these set of images, the change in coloration and radial features between pressurized oxygen and ambient air conditions are evident. A homogeneous teal region associated with m-MoO$_2$/o-Mo$_4$O$_{11}$/o-Mo$_{18}$O$_{52}$ phases is observed in the images corresponding to pressurized oxygen at 16 psig and 0.53 mJ/cm^2 (last row) of Fig. 4. In contrast, the images corresponding to ambient air atmosphere and 0.53 mJ/cm^2 (third row) of Fig. 4 show the radial regions II and IV detailed in Fig. 2. In general, images from Fig. 4 suggest that the MoO$_3$ obtained in the center of the irradiated area is the result of re-oxidation of MoO$_2$ to MoO$_3$ rather than a direct oxidation of molybdenum into MoO$_3$.

To compare the spatial features of the obtained results, two main characteristic radii can be extracted from the regions described in Fig. 2 and Fig. 3. An inner radius (r_i) corresponding to the circular central region (region I) and an outer radius (r_o) corresponding to the total modified area (region IV). From Fig. 2 one can infer that r_i is related mainly to the area of transformed α-MoO$_3$ while the difference r_o-r_i is related to the area with a predominant content of m-MoO$_2$. We found that the spatial extent of r_o and r_i was the main difference between ambient air and pressurized oxygen oxidation compound formation. In general, we have observed that r_o and r_i depend on the laser fluence, irradiation time and ambient conditions. Figure 5 summarizes the inner and outer radius measured from the optical micrographs shown in Fig. 4.
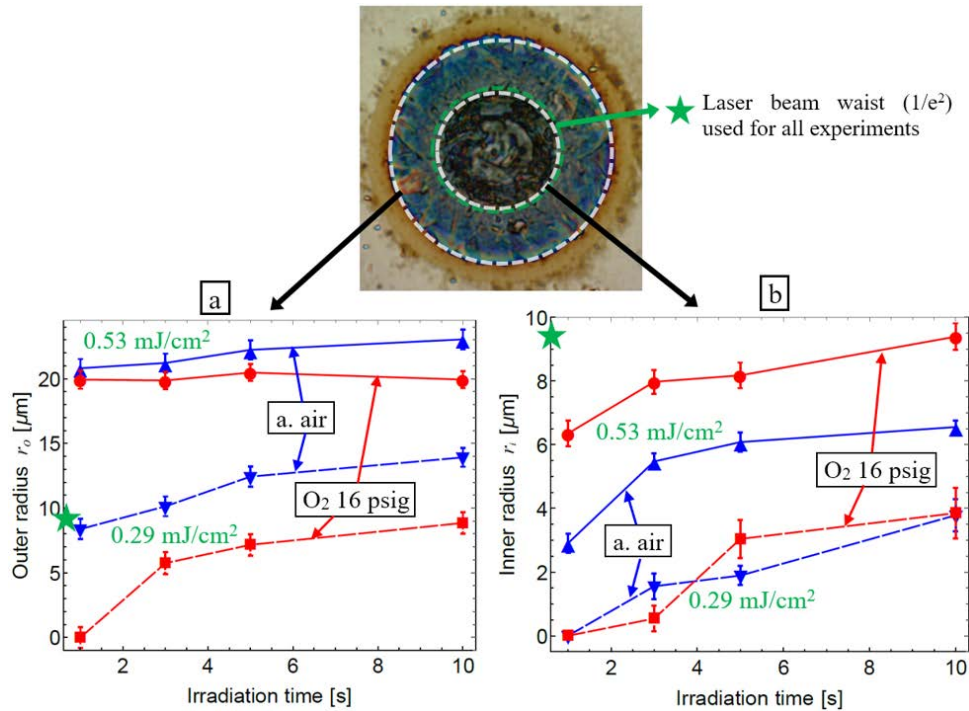
Fig. 5. Outer (a) and inner (b) radius of the samples shown in Fig. 4. A representative micrograph has been used to indicate the corresponding plots for the inner/outer radius. Blue symbols correspond to ambient air conditions while red symbols correspond to 16 psig pressurized oxygen conditions. Dashed lines correspond to 0.29 mJ/cm^2 and solid lines correspond to 0.53 mJ/cm^2 of fluence. The laser beam radius has been indicated with a green star in both panels. Error bars represent the standard deviation from 3 radial measurements.

Figure 5 shows the outer and inner radius as a function of irradiation time for two different laser fluences (0.29 and 0.53 mJ/cm^2) and two different pressure conditions (ambient air and 16 psig pressurized oxygen). Four sets of experimental data points are depicted in Fig. 5(a) which correspond to the outer radii as a function of irradiation time from 4 different irradiation conditions. Two data sets in Fig. 5(a) correspond to a fluence of 0.29 mJ/cm^2 and are joined with dashed lines, while the two sets of data corresponding to 0.53 mJ/cm^2 are joined with solid lines. Additionally, in Fig. 5(a) we have used blue lines to designate ambient air irradiation condition and red lines to designate irradiation performed at 16 psig pressurized oxygen. Similarly, Fig. 5(b) shows the inner radius as a function of irradiation time with the same designation scheme used in Fig. 5(a) (dashed lines: 0.29 mJ/cm^2, solid lines: 0.53 mJ/cm^2, blue lines: ambient air, red lines: 16 psig). As seen in Fig. 5(a), the outer radius for 0.29 mJ/cm^2 (dashed lines in Fig. 5) and for 0.53 mJ/cm^2 (solid lines in Fig. 5) is larger for the case of ambient air conditions (blue symbols in Fig. 5). This behavior is observed over all the irradiation times studied for these samples. The unexpected reduction of the laser-induced modified area in an oxygen-rich atmosphere is one of the main findings of this experimental study. In contrast, the inner radii obtained by laser irradiation at 0.53 mJ/cm^2 in 16 psig pressurized oxygen (red solid symbols in Fig. 5(b)) were larger than their counterpart irradiated in ambient air conditions (blue solid symbols in Fig. 5(b)). A smaller outer radius combined with a larger inner radius means that the ratio of transformed α-MoO$_3$ area over the total modified area (r_i^2 / r_o^2) is considerable higher for the case of laser irradiation in pressurized oxygen conditions (about 3 times greater for 0.53 mJ/cm^2 after 10 s). However, for the case of lower fluence (0.29 mJ/cm^2), the inner radii obtained in ambient air conditions (blue dashed line in Fig. 5(b)) and the ones obtained in 16 psig pressurized oxygen conditions

(red dashed line in Fig. 5(b)) are very similar and no clear tendency can be observed over the irradiation times performed in these experiments. For 3 seconds of irradiation time the inner radius obtained in ambient air condition was higher than for pressurized oxygen, but for 5 seconds of irradiation time the inner radius for pressurized oxygen surpassed the inner radius obtained in ambient air. At 10 seconds of irradiation time both radii showed similar lengths. This behavior may be the result of a complex interplay among the mechanisms involved in light absorption and heat transfer in the surface of the thin film.

Notice that the inner radii shown in Fig. 5(b) correspond to a region that lies completely inside the laser irradiated area (beam radius of 9.5 μm, indicated with a green star in Fig. 5(a) and 5(b)). Furthermore, Fig. 5(b) suggests a potential fine tuning on the extent of the α-MoO$_3$ region by controlling the experimental irradiation time. This means that some of the microstructures observed may be related with the gaussian shape of the laser beam. Nevertheless, most of the outer radii shown in Fig. 5(a) correspond to regions outside the laser irradiated area. We have observed that the modification area extends up to 3 times farther the laser beam radius which in turn suggests that the outer modification area is related with heat conduction processes. These results suggest that the modification mechanism in the inner area is related to direct irradiation of the laser beam to the surface of the sample while the modification mechanism of the outer area is related mainly to heat diffusion effects. A larger modification area as compared to the laser irradiation area has been reported before in femtosecond laser processing [45].

In general, once the laser and material parameters are given, the amount of absorbed energy is known, and the spatial and temporal profiles can be calculated. Then, one could potentially relate the temporal and spatial calculations of the absorbed heat with the experimental results with by means of a laser-induced modification rate. The two-temperature model is the most widely used approach which relies on solving a system of two heat conduction equations coupled by the electron-phonon coupling constant [46,47]. According to a recent work on femtosecond laser irradiation of molybdenum thin films [47], the molybdenum thin film reaches a temperature of 9000 K at the end of a single femtosecond pulse. Although this temperature is much higher than the reported melting point for molybdenum (700-800 °C [48]), the model in [47] show no insight about the laser-induced heating due to multiple femtosecond laser pulses. On the other hand, a heat-accumulation model proposed by Weber et. al [49] has shown that the temperature increase due to multiple pulses may lead to a finite temperature. According to this model and using typical values of laser and material properties from the present work (density = 10.28×10^3 kg/m^3, specific heat capacity = 250 J/(kg K), thermal diffusivity = 4.7×10^{-5} m^2/s, reflectivity = 70% [50], repetition rate = 54.7 MHz, fluence = 2.14 mJ/cm^2) the temperature increase converges to 140 °C. Similarly, a corresponding cw laser with the same average power irradiating on a semi-infinite solid (see Eq. (3).17 in [51]) leads to a steady state temperature of 130 °C. These two temperatures seem low even to generate oxidation from Mo to MoO$_2$ which has been reported to initiate at around 500 °C [50]. In general, this means that a model that accurately describes the spatial and temporal profiles of the temperature induced by a femtosecond laser pulse train in experimental-related time and space scales is yet to come and more work is needed to elucidate the mechanisms that govern this intriguing modification processes.

3.3 Influence of oxygen pressure and fluence on laser-induced oxidation

Light micrographs of Mo thin films irradiated with different fluences (shown in rows) and different oxygen pressures (shown in columns) at a fixed irradiation time of 10 seconds are shown in Fig. 6. As was pointed out previously, similar regions as defined in Fig. 2 are observed for the different experimental conditions studied here. A sharper coloration annuli transition is evident in the irradiations performed in pressurized oxygen gas conditions, which may be the result of a larger temperature gradient during laser irradiation. As expected, for all ambient conditions studied here the area of the modified regions increases as fluence

increases (compare top to bottom images in each column of Fig. 6). Interestingly, when comparing irradiations in ambient air (first column in Fig. 6) to irradiations performed in higher oxygen pressure (columns 2-5 in Fig. 6) a smaller overall modified area is observed for irradiations performed in pressurized oxygen atmosphere. This is very evident in the top row of Fig. 6 which corresponds to a fluence of 0.29 mJ/cm^2. Images from Fig. 6 along with the SEM images of Figs. 2(c) and 2(d) suggest a crater-like structure in the inner modified regions. Furthermore, elevations over the initial level of the thin films at region II were corroborated by means of FIB cuts as shown in Fig. 7(a) (ambient air, 0.53 mJ/cm^2, 10s) and Fig. 7(b) (8 psig pressurized oxygen, 0.53 mJ/cm^2, 10s). A notable depression in region I was also observed in FIB cut SEM images. Elevations in MoO_2 regions are expected as the modification of Mo to MoO_2 results in an increase of mass and volume. On the other hand, smaller thickness on the inner modified region may be related with evaporation or sublimation of material as the oxidation of MoO_2 to MoO_3 and volatilization of MoO_3 occur simultaneously in the temperature range of 650-750 °C [50,52,53].
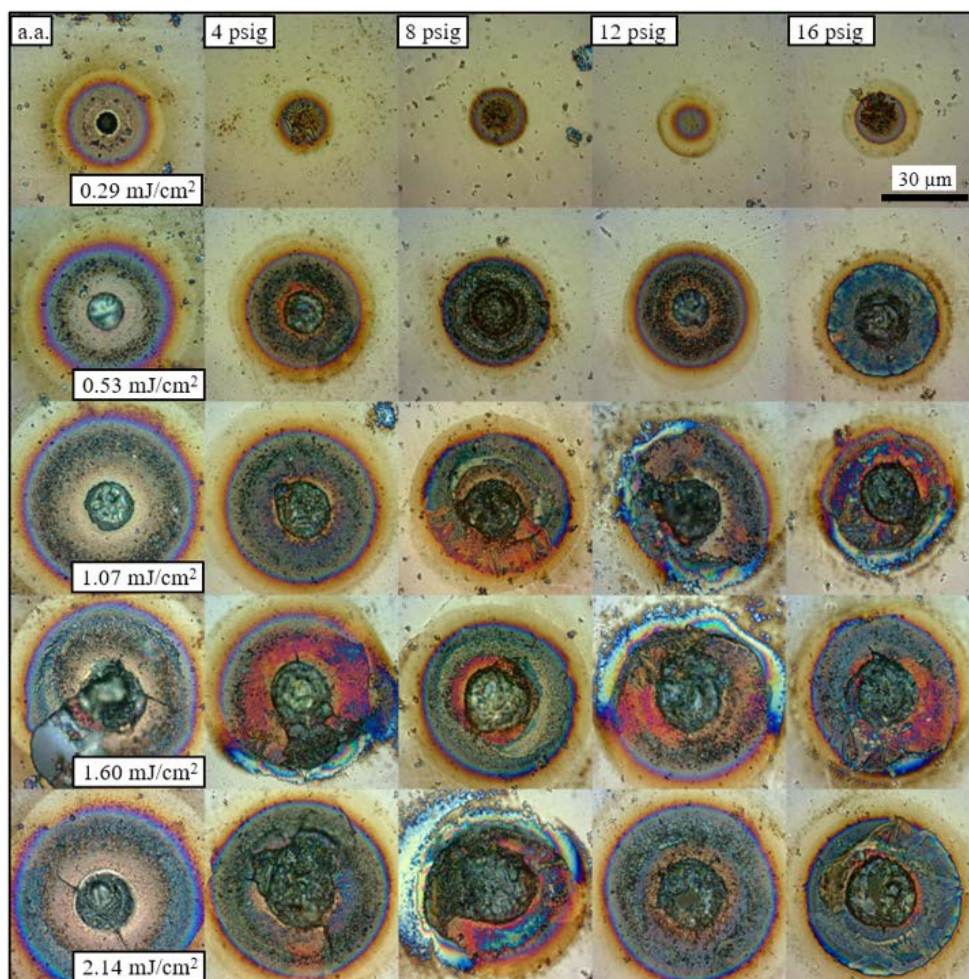

Fig. 6. Light micrographs of molybdenum thin films irradiated at different fluences and with different atmospheric conditions. First column: molybdenum thin films irradiated in ambient air (a. a.) with fluences between 0.29 and 2.14 mJ/cm^2. Second to fifth columns: molybdenum thin films irradiated in pressurized oxygen at 4, 8, 12, 16 psig and fluences between 0.29 and 2.14 mJ/cm^2. The irradiation time for all the images shown was 10 s. All images are shown at the same scale.

As seen in Fig. 7, delamination is observed for the sample irradiated in ambient air while a radial step-like structure is observed for the case of pressurized oxygen irradiation conditions. Moreover, the thinner inner section shown in Fig. 7(b) indicates a higher amount of evaporated material than the evaporated material for the case of irradiation in ambient air. Notice that the irradiated films shown in Figs. 7(a) and 7(b) were irradiated with the same fluence and same irradiation time, thus we would expect the same amount of energy deposited in the thin films for both cases. Therefore, the higher production of MoO_3 for the case of pressurized oxygen conditions may be related with a larger number of oxygen molecules available in the surroundings as well as with a higher diffusion rate of oxygen within the thin film volume.
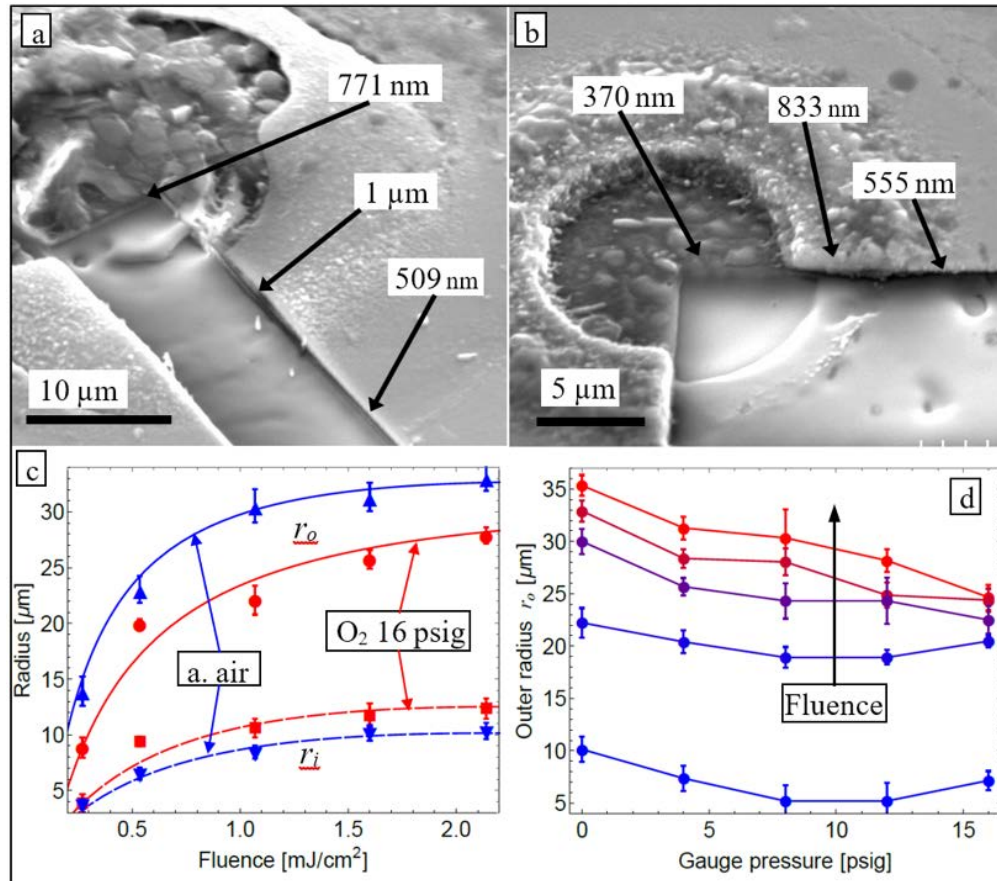
Fig. 7. SEM images of FIB cuts of irradiated molybdenum thin film at ambient air conditions (a) and pressurized oxygen at 8 psig (b). A crater-like morphology is clearly seen as different highs were measured along the cut. c) Inner (dashed line) and outer (solid line) radius as a function of fluence for two different ambient conditions: ambient air (blue symbols) and oxygen at 16 psig (red symbols). Lines are just a guide to the eye. d) Outer radius as a function of gauge pressure for different fluences and 5 s irradiation. In panel d) zero gauge pressure corresponds to ambient air conditions. The top (light red) curve corresponds to the highest fluence (2.14 mJ/cm²) while the bottom (light blue) curve corresponds to the lowest fluence studied in this work (0.29 mJ/cm²).

Figure 7(c) shows the inner and outer radius as a function of fluence for laser irradiations performed in ambient air and pressurized oxygen at 16 psig for a fixed irradiation time of 10 s. With greater oxygen pressure, a larger oxidized area from the same laser irradiation conditions is expected. As the density of oxygen increases, the amount of adsorbed oxygen

molecules also increases leading to a higher concentration of oxygen diffusion into vacancy sites. Thus, one may expect a more widespread laser-induced oxidation area for pressurized oxygen conditions. Unexpectedly, an increase in oxygen pressure reduces the overall modified laser-induced oxidation area. Nevertheless, the inner modified region for irradiations performed in pressurized oxygen conditions were slightly larger than the ones performed in ambient air. This means that the ratio of MoO_3 modified area to total modified area is higher when irradiating in an oxygen rich atmosphere than when irradiating in ambient air. As ambient conditions do not change molybdenum properties such as density or specific heat capacity and only small changes in thermal conductivity of metals have been reported in ambient pressures as high as GPa [54] a possible explanation for a reduced modified region in pressurized oxygen conditions should come from the altered solid-fluid interface (Mo-Air/O_2).

A reduction on the femtosecond laser-induced ablation diameter on copper for increasing pressure has been reported recently [55]. However, the fluences studied in Ref [55]. (~10 J/cm^2) are well above the single-pulse ablation threshold of copper whereas the present study shows laser-modifications performed with fluences in the range of few mJ/cm^2, which is well below the single-pulse ablation threshold of molybdenum. On the other hand, heat transfer across solid-fluid interface at nanoscale and microscale has shown to behave very different from the macroscopic scale and to be highly dependent on the pressure and flow conditions of the surrounding fluid [37,56]. As spatial scale decreases, pressure can cause important heat losses at the solid-liquid interface [56]. In other words, convection can become relatively significant when compared to conduction at microscales and nanoscales. In laser irradiation of thin films, higher pressures may lead to a higher oxygen diffusion rates, but also higher pressures can result in a higher convective heat loss due to a larger number of gas molecules moving heat away faster from the surroundings of the irradiated area. Figure 7(d) depicts the outer radius as a function of gauge pressure for different fluences at a fixed irradiation time of 5 s. We have chosen the outer radius to show the behavior over pressure because the outer radius presented more significant changes with pressure as it was shown in Fig. 7(c). The fact that the outer radius exhibits a more pronounced dependence on pressure agrees with the assumption of heat diffusion effects as the mechanism responsible for modification outside the laser irradiation area.

4. Conclusions

Data from Fig. 7(d) seems to support the hypothesis that the effect of a pressurized oxygen atmosphere results in a combination of competing mechanisms facilitating (more oxygen adsorption) and delaying (increased micro scale convection) oxidation. Notably, the corresponding curves for 2.14, 1.60 and 1.07 mJ/cm^2 in Fig. 7(d) (light red, dark red and purple lines, respectively) show that outer radius has a tendency of decreasing as gauge pressure increases. Interestingly, the corresponding curves for 0.53 and 0.29 mJ/cm^2 (dark blue and light blue lines, respectively) show a decrease in outer radius from 0 to 8 psig and an increase in outer radius for 12 and 16 psig. These increased outer radii at relatively high oxygen pressure and low fluence may represent the transition where increased oxygen adsorption dominates increased micro scale convection. This in general shows that the total modification area is a function of laser fluence, irradiation time as well as oxygen pressure. We can speculate on two main effects of the pressurized oxygen conditions on the laser-induced oxidation of molybdenum thin films: 1) Oxygen can have higher convection than ambient air at small scales. An oxygen rich atmosphere at micrometer scale heated areas can impose a higher amount of thermal energy per unit area per unit time that is being extracted from the surface of the thin film. This can be the reason for the delayed appearance of modified regions shown in Fig. 4 and the shorter outer radii compared to ambient air conditions shown in Figs. 5 and 6; and 2) MoO_3 formation is enhanced in the laser spot area by increased oxygen diffusion rate, which is due to higher oxygen pressure. Therefore,

convection losses may be higher, but there is more oxygen present to drive diffusion resulting in smaller total oxidation area but larger highly oxidized (MoO_3) center area.

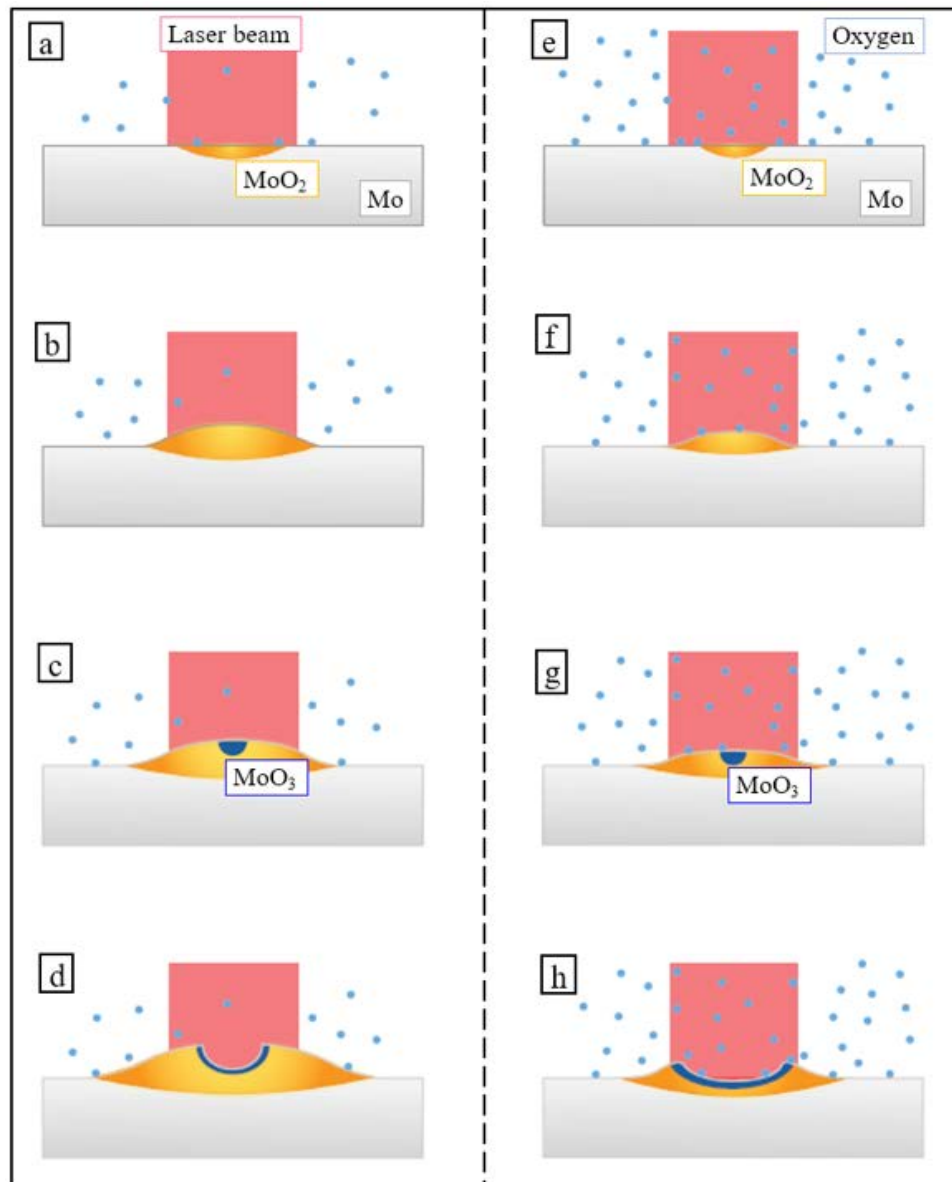
Fig. 8. Schematic representation of the laser-induced oxidation of the molybdenum films. For simplicity, only the two most abundant oxides (MoO_2 and MoO_3) are depicted. The case of ambient air conditions is shown in a, b, c and d whereas pressurized oxygen condition is shown schematically in e, f, g and h. During the first microseconds of laser irradiation (a, e) a region of MoO_2 appears. Then, the MoO_2 region increases in mass and volume forming an elevation over the film (b, f). The appearance/growing of the MoO_2 region for the case of pressurized oxygen condition is delayed/decreased due to a higher amount of heat extracted by convection. After a few milliseconds, the energy deposited in the film allows for a re-oxidation of MoO_2 to MoO_3 at the center of the laser beam (c, g). Then, volatilization of MoO_3 occurs due to the low volatilization temperature of MoO_3 [50,52,53] (d, h). Once the energy deposited in the film is much higher than the energy extracted by convection, the pressurized oxygen condition permits a broader re-oxidation of MoO_3.

A higher diffusion rate of oxygen molecules into the Mo thin film may enhance oxidation once the heat deposited in the surface of the thin film is higher than the heat extracted from the surface by the surrounding oxygen molecules. In other words, the pressurized oxygen conditions impose a higher energy threshold for the oxidation to occur due to convection; but once the energy threshold is surpassed, the oxidation processes becomes more efficient than in air ambient conditions due to more adsorbed oxygen molecules. This energy threshold condition is more likely to occur within the 9.5 µm laser spot radius where the metal surface absorbs the laser energy. The morphologies shown in Figs. 7(a) and 7(b) also agree with this hypothesis as more evaporated material implies that more energy was used to change phase and lost to evaporation and/or sublimation causing less heat to be diffused to the outer areas. Although this simple description seems to agree with the results shown here, a more complete description must consider effects such as nonlinear absorption, electron-phonon heat coupling and the fact that as molybdenum changes to MoO_3 the absorption coefficient decreases dramatically due to the higher transparency of MoO_3. From the results presented here, it is evident that more work is needed to unveil the intricated interaction of ultrashort laser pulses with metal interfaces and that the effect of microscale and nanoscale convection on material modification by means of femtosecond laser must be considered from experimental and theoretical points of view.